Check for updates

Polyimide-based graphene composite foams with hierarchical impedance gradient for efficient electromagnetic absorption†

Lei Pu,[a] Shuangshuang Li,[a] Yawei Zhang,[a] Haiyan Zhu,[a] Wei Fan, [ID][b] Piming Ma, [ID][a] Weifu Dong, [ID][a] Zicheng Wang [ID]*[a] and Tianxi Liu*[a]

The development of high-performance microwave absorption materials with strong absorption capacity and broad bandwidth is highly desirable in the field of electromagnetic pollution protection. Herein, polyimide/graphene composite foam with a multi-hierarchical impedance gradient structure has been precisely designed and controllably constructed by two-step vacuum impregnation, which effectively facilitates further attenuation of electromagnetic waves entering the graphene skeleton due to the generation of interfacial polarization relaxation and internal multiple reflection/scattering, thereby endowing it with excellent broadband microwave absorption performance. Meanwhile, the microwave absorption performance can be controllably adjusted by optimizing the impedance gradient of the skeleton. As a result, the optimized PI–GP–rGO composite foam exhibits a minimum reflection loss of -32.87 dB with an effective bandwidth of 6.22 GHz (8.26–14.48 GHz) at 10.39 GHz when the thickness is 4.0 mm.

Introduction

With the development of information technology, a series of new electronic devices have shown explosive growth. Over time, electromagnetic radiation has become a new source of environmental pollution, which not only seriously affects the control of the electronic equipment, but also endangers the health of the organisms.[1–3] In addition, the continuous development of military radar has put forward higher requirements for weapons and equipment to avoid electronic reconnaissance and improve survivability on the battlefield. Therefore, the development of high-performance microwave absorption (MA) materials with a strong absorption capacity and a broad bandwidth has become particularly urgent in the field of electromagnetic pollution protection and radar stealth.[4–11]

In the past few years, porous carbon materials have been widely used in the field of electromagnetic protection due to their porous or hollow microstructure and the excellent electrical conductivity of skeletons.[12–17] Because of the presence of the porous structure, random electromagnetic

reflection/scattering would repeatedly occur at the interfaces of the cell wall, resulting in the transfer of electromagnetic energy to be dissipated as heat in the form of microcurrent. For example, Song *et al.* prepared a highly ordered porous carbon (HOPC) material and the minimum reflection loss (RL_{min}) value of the HOPC/wax composite reaches -18 dB at 13 GHz.[18] Wang *et al.* used the coal liquefaction residue as a carbon source to synthesize three-dimensional (3D) carbon foam through a simple template method.[19] The sample exhibited a broad effective absorption bandwidth ($RL < -10$ dB) of up to 5.8 GHz. However, to date, porous carbon-based MA materials mainly rely on the multiple reflections between pore structures to achieve attenuation of incident electromagnetic waves (EMWs), and rarely involve the effect of impedance distribution/gradient on the dissipation of electromagnetic waves entering the conductive skeleton.[20–24]

In this work, polyimide/graphene composite foam with a multi-hierarchical impedance gradient structure has been precisely designed and controllably constructed by two-step vacuum impregnation. Due to the superior thermal stability and mechanical strength, polyimide (PI) foam is employed as a 3D porous skeleton and subsequently coated with reduced graphene oxide/polyimide (GP) and reduced graphene oxide (rGO) as the second and third layers, respectively, resulting in the PI–GP–rGO composite foam. The multi-hierarchical structure leads to the formation of a three-level impedance gradient, which effectively facilitates further attenuation of electromagnetic waves entering the graphene skeleton due to

[a] *The Key Laboratory of Synthetic and Biological Colloids, Ministry of Education, Institute of Nanocomposites and Energy Materials, School of Chemical and Material Engineering, Jiangnan University, 214122 Wuxi, Jiangsu, P. R. China. E-mail: wangzc@jiangnan.edu.cn, txliu@jiangnan.edu.cn*

[b] *State Key Laboratory for Modification of Chemical Fibers and Polymer Materials, College of Materials Science and Engineering, Donghua University, Shanghai 201620, P. R. China*

† Electronic supplementary information (ESI) available. See DOI: 10.1039/d0tc04951d

the generation of interface polarization and internal multiple reflection/scattering, thereby endowing the composite foam with excellent broadband microwave absorption performance in comparison with the monotonous graphene foam. Meanwhile, the microwave absorption performance can be effectively adjusted by controlling the impedance gradient of the skeleton.

Experimental

Materials

Graphite powder (325 mesh) was obtained from Qingdao Jin Ri Lai Graphite Co. Ltd (Qingdao, China). Concentrated sulfuric acid (H_2SO_4, 98%), phosphoric acid (H_3PO_4), hydrochloric acid (HCl, 37%), potassium permanganate ($KMnO_4$, $\geq$99.5%), pyromellitic dianhydride (PMDA, $\geq$98.5%), 4,4′-oxydianiline (ODA, $\geq$98.0%), triethylamine (TEA 99%) and N,N-dimethylacetamide (DMAc, 99%) were purchased from Sinopharm Chemical Reagent Co., Ltd. All commercial reagents in this study were of analytical grade and used without further purification.

Synthesis of graphene oxide (GO) and polyamide acid (PAA)

Graphite flakes were oxidized using the improved Hummers' method.[25,26] Water-soluble poly(amic acid) (PAA) was prepared through the condensation polymerization reaction of PMDA and ODA in an equimolar ratio using DMAc. Then, TEA was used as the hydrophilic surface modifier to prepare PAA salt. The viscous liquid was decanted with deionized water and repeatedly washed to remove the solvent and unreacted raw materials. After freeze-drying, the water-soluble PAA was obtained.

Preparation of polyimide/graphene composite foams with a hierarchical structure

As shown in Scheme 1, 0.15 g of TEA and 0.3 g of PAA were fully dissolved in 10 mL of deionized water to obtain a PAA sol which was then kept at 4 °C for 24 h to obtain the PAA hydrogel. The PAA hydrogel was freeze-dried and heat-treated at 300 °C for 2 h to complete the imidization process and obtain the PI foam.

The PI foam was used as a skeleton and vacuum-impregnated with a mixed solution of GO/PAA at different concentration ratios. Subsequently, the mixture was taken out for the same freeze-drying and heat treatment to obtain the composite foam with a

Table 1 Composition of polyimide/graphene composite foams

No.	GO:PAA (mg mL^{-1})	Name (bilayer)	GO (mg mL^{-1})	Name (trilayer)
1	0:0	PI	0	PI
2	0:4	PI–PI	4	PI–PI–rGO
3	4:8	PI–GP$_{1/3}$	4	PI–GP$_{1/3}$–rGO
4	4:4	PI–GP$_{1/2}$	4	PI–GP$_{1/2}$–rGO
5	4:2	PI–GP$_{2/3}$	4	PI–GP$_{2/3}$–rGO
6	4:0	PI–rGO	4	PI–rGO–rGO

bilayer structure (PI–GP$_x$, where x represents the content of GO in GO/PAA, as displayed in Table 1). Then, the PI–GP$_x$ was immersed in GO dispersions of 4 mg mL^{-1} using the vacuum impregnation process. Finally, the mixture was taken out for freeze-drying and thermal treatment to obtain the multi-hierarchical composite foam with a trilayer structure (PI–GP$_x$–rGO). Here, rGO refers to reduced graphene oxide originating from the thermal reduction of GO.
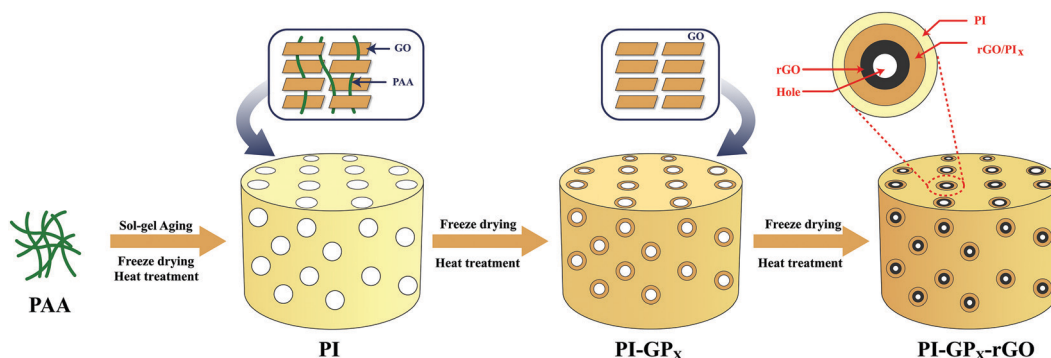
Characterization

Scanning electron microscopy (SEM) images were taken with a Hitachi S-4800 cold field-emission scanning electron microscope operated at 30 kV. X-ray diffraction (XRD) patterns were collected using a Bruker D8 X-ray diffractometer with a Cu Kα X-ray source ($\lambda = 1.5418$ Å). Thermal gravimetric analysis (TGA) was carried out by using a TGA/DSC1/1100SF system under a N_2 atmosphere at a heating rate of 10 °C min^{-1}. The mechanical properties were recorded using an electronic universal testing machine (UTM2203, load cell = 200 N, Shenzhen Suns Technology Stock Co. Ltd, China), and the results are exhibited in Fig. S9 (ESI†). The electromagnetic parameters of the foams were measured using a vector network analyzer (Agilent 8720ET) at 0.5–18 GHz. The testing samples were fabricated by vacuum impregnation with melting paraffin and cut into standard coaxial rings with an outer diameter of 7.0 mm and an inner diameter of 3.0 mm, and the percentage of paraffin in the samples was ∼85 wt%.

Results and discussion

Structure and morphology of composite foams

The SEM images of composite foams are shown in Fig. 1. An isotropic macroporous structure for PI foam with an average

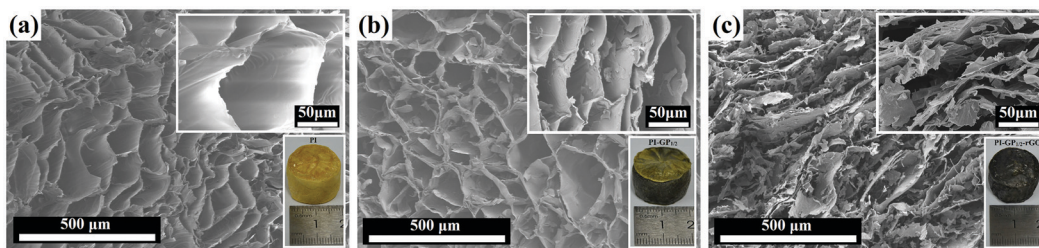**Scheme 1** Preparation of PI–GP$_x$–rGO composite foams with a multi-hierarchical structure.

This journal is © The Royal Society of Chemistry 2021

J. Mater. Chem. C, 2021, **9**, 2086–2094 | **2087**

Fig. 1 SEM images of polyimide/graphene composite foams with different hierarchical structures: (a) PI; (b) PI–GP$_{1/2}$; and (c) PI–GP$_{1/2}$–rGO (The small picture embedded in the upper right corner is a partial magnification of 500 times).

pore size of *ca.* 100 μm can be obviously observed in Fig. 1(a). Meanwhile, the pore size of PI–GP$_{1/2}$ and PI–GP$_{1/2}$–rGO gradually decreases as displayed in Fig. 1(b) and (c), respectively, which can be ascribed to the effective loading of GO/PAA and GO, thereby visually confirming the successful construction of the hierarchical skeleton structure. Moreover, the lamellar structure in the pores of PI-GP$_{1/2}$ and PI–GP$_{1/2}$–rGO becomes much more obvious (Fig. 1 and Fig. S1, ESI†). The growth of ice crystals is guided orderly by the rigid GO nanosheets on the pore walls of composite foams along the interlayer during freeze-drying.[27] In addition, the GO nanosheets begin to bend and be stacked into layers when the oxygen functional groups of GO are removed during the thermal treatment.[28,29] As a result, the morphology of PI–GP$_{1/2}$–rGO exhibits a distinctive lamellar structure in comparison with those of PI and PI–GP$_{1/2}$. Other PI–GP$_x$ and PI–GP$_x$–rGO with different GO contents exhibit similar morphology as shown in Fig. S2 (ESI†), which once again verifies the controllable construction of composite foams with a hierarchical structure.

TGA was employed to explore the microstructural changes of GO sheets and PAA chains in the composite foams. As shown in Fig. 2(a)–(c), after thermal treatment at 300 °C for 2 h, the thermal stabilities of GO, PAA and GO/PAA exhibit significant improvement. It can be attributed to the decomposition of unstable functional groups in GO sheets and the dehydration of PAA chains, thereby confirming the effectiveness of the thermal treatment on the thermal reduction of GO sheets and the imidization of PAA chains. Furthermore, the thermal stability of composite foams has been prominently enhanced after rGO/ PI and rGO are loaded on PI and PI–GP$_{1/2}$. As depicted in Fig. 2(d), the initial decomposition temperatures ($T_{5\,wt\%}$, corresponding to the temperature with a 5% weight loss) of PI, PI–GP$_{1/2}$ and PI–GP$_{1/2}$–rGO are 487.9 °C, 517.7 °C and 526.3 °C, respectively. At the same time, the residual yields of PI, PI–GP$_{1/2}$ and PI–GP$_{1/2}$–rGO are 49.9 wt%, 52.3 wt% and 56.4 wt% at 800 °C, respectively. In addition, for PI–GP$_x$ and PI–GP$_x$– rGO composite foams with different GO contents in GO/PAA$_x$ of the second layer, similar tendency for $T_{5\,wt\%}$ and residual yield can be observed in Fig. S3 (ESI†). As shown in the SEM observation (Fig. 1), rGO/PI and rGO are uniformly distributed on the surface of the composite foams. Moreover, the rGO sheets exhibit good thermal stability, which can protect the foam skeleton from being decomposed too fast during the thermal treatment.[29,30] More importantly, the large evolution in

thermal stability indirectly confirms that the multi-hierarchical skeleton structure has been successfully constructed in the composite foams.

The microstructural changes produced during the thermal treatment could be also identified by XRD. As shown in Fig. 3(a), GO powder exhibits a sharp diffraction peak indexed to (002) centered at 10.8°. After incorporation with PAA, a well-defined diffraction peak of the obtained GO/PAA$_{1/2}$ shifts to a lower angle of 8.3°. Moreover, the characteristic peak of PAA shifted from 17.0° to 16.6°, which can be obviously observed in Fig. 3(c),[31,32] indicating that the introduction of PAA chains facilitates exfoliation of GO sheets effectively. After being treated at 300 °C, the stacking peak of GO disappears, while a new broad peak at around 23.9° arises as shown in Fig. 3(c), corresponding to the (001) plane of reduced graphene oxide (Fig. 3(a)), which also verifies the effectiveness of the thermal treatment on the reduction of GO in the GO/PAA$_{1/2}$ system. Meanwhile, it is worth noting that the characteristic peak of the obtained PI in rGO/PI shifts to a lower angle of ∼15.0°. For the composite foams with a hierarchical structure, the diffraction peak (17.1°) of PI in PI–GP$_{1/2}$ exhibits a superimposed effect of PI (17.9°) and rGO/PI$_{1/2}$ (∼15.0°) as shown in Fig. 3(d), indicating the successful construction of bilayer composite foams. In comparison with pure PI foam, a new shoulder peak (located at ∼25.0°) in PI–GP$_{1/2}$ can be attributed to the characteristic diffraction of graphene. For the PI–GP$_{1/2}$–rGO, the shoulder peak strengthens, whereas the characteristic peak of PI weakens due to the loading of the third-layer rGO on the surface of the PI–GP$_{1/2}$ foam, demonstrating the successful construction of multi-hierarchical composite foams. Furthermore, the other PI–GP$_x$ and PI–GP$_x$–rGO with different GO contents exhibit similar results as shown in Fig. S4 (ESI†), which once again verifies the controllable construction of composite foams with a hierarchical structure.

Permittivity properties of composite foams

The MA characteristics of non-magnetic absorbing materials are highly dependent on their permittivity parameters as shown in Fig. 4 and Fig. S5 (ESI†). Among the complex permittivity ($\varepsilon_r = \varepsilon' - j\varepsilon''$), the real part ε' represents the storage modulus of the MA materials, while the imaginary part ε'' represents the loss modulus of the MA materials.[33] Fig. 4(a)–(c) show the gradually increasing complex permittivity (ε', and ε'') and dielectric loss tangent (tan $\delta_\varepsilon = \varepsilon''/\varepsilon'$) of PI, PI–GP$_{1/2}$, and PI–GP$_{1/2}$–rGO in the

2088 | *J. Mater. Chem. C*, 2021, **9**, 2086–2094

This journal is © The Royal Society of Chemistry 2021
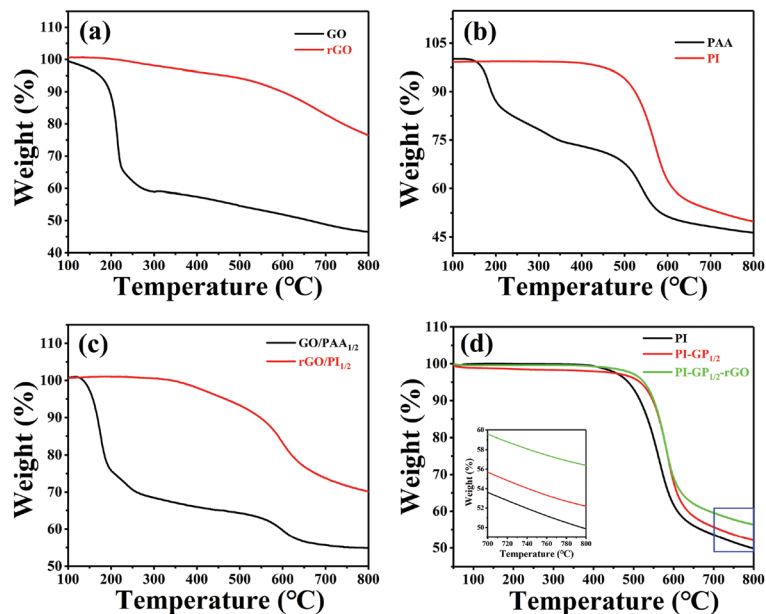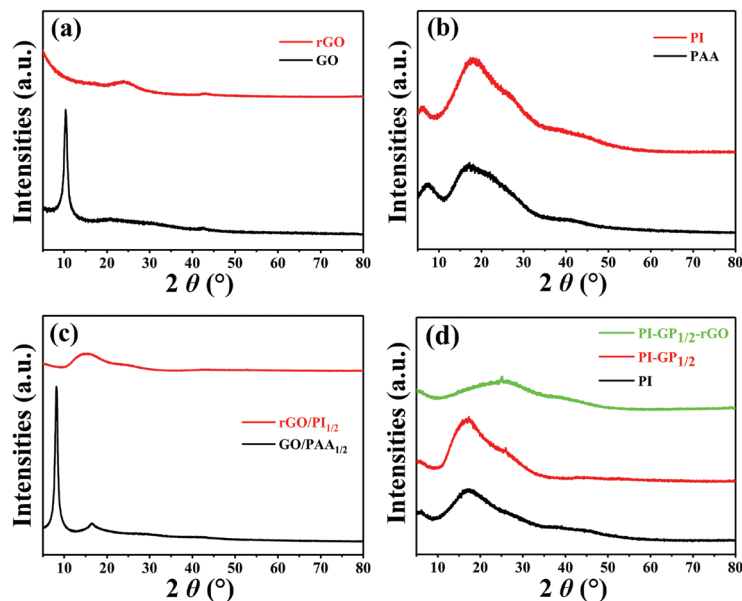
Fig. 2 TGA curves of (a) GO and rGO, (b) PAA and PI, and (c) GO/PAA$_{1/2}$ and rGO/PI$_{1/2}$; (d) polyimide/graphene composite foams with different hierarchical structures: PI, PI–GP$_{1/2}$, and PI–GP$_{1/2}$–rGO.

Fig. 3 (a) XRD curves of (a) GO and rGO, (b) PAA and PI, and (c) GO/PAA$_{1/2}$ and rGO/PI$_{1/2}$; (d) polyimide/graphene composite foams with different hierarchical structures: PI, PI–GP$_{1/2}$, and PI–GP$_{1/2}$–rGO.

frequency range of 0.5–18 GHz, verifying the formation of the three-level impedance gradient of multi-hierarchical composite foams. Meanwhile, the impedance gradient of PI–GP$_x$–rGO can be controllably adjusted by optimizing the permittivity properties of GO/PAA$_x$ with different GO contents in the second layer, as shown in Fig. 4(d)–(f). It is worth noting that the permittivity of PI–GP$_{1/2}$ and PI–GP$_{1/2}$–rGO is higher than that of pure rGO, which can be attributed to the successive pushing of the growth of ice crystals

during the freeze-drying process, leading to the formation of more compact graphene conductive networks in PI–GP$_{1/2}$ and PI–GP$_{1/2}$–rGO.

In order to further identify the factors contributing to the permittivity properties, the plots of ε'' *versus* ε' (Cole–Cole semicircles) for the composite foams are shown in Fig. S6 (ESI†). As for PI foam, there are several semicircles in Fig. S6(a) (ESI†), indicating the existence of orientation polarization processes in polyimide chains. After incorporation
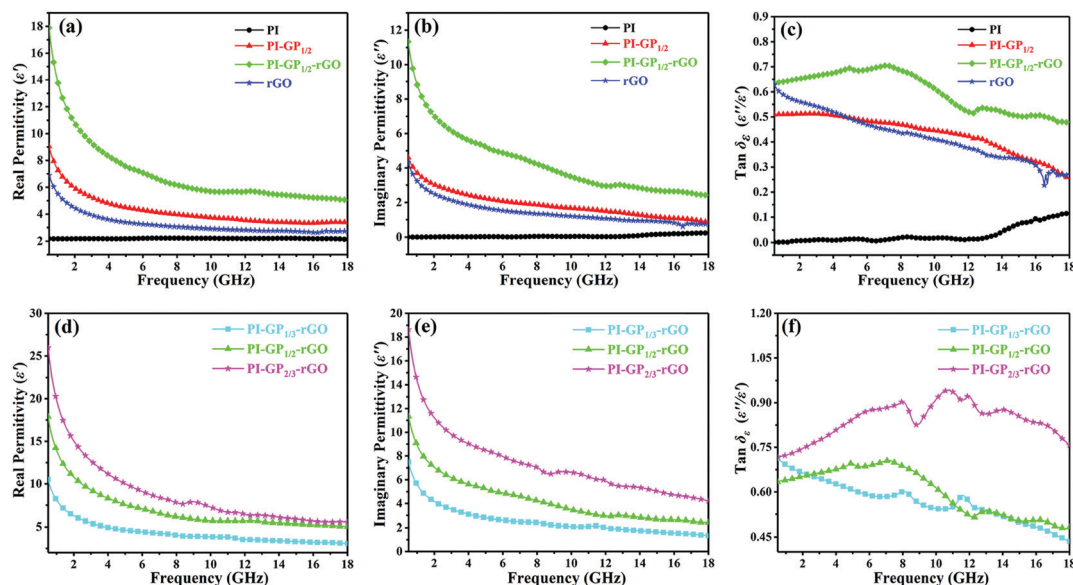
Fig. 4 The electromagnetic parameters of the composite foams: (a and d) the real parts of complex permittivity; (b and e) the imaginary parts of complex permittivity; and (c and f) the dielectric loss tangent of the composite foams.

with $rGO/PI_{1/2}$, the plot of $PI–GP_{1/2}$ exhibits multiple semicircles distinguished from PI foam, which may be caused by the interface polarization relaxation existing in the $rGO/PI_{1/2}$ as well as between PI and $rGO/PI_{1/2}$, being beneficial to the attenuation of microwave energy. Moreover, it is worth noting that conductivity loss can be also confirmed by the presence of the line tail in the plot (Fig. S6(b), ESI†), which mainly arises from the formation of a conductive rGO network in the second layer for $PI–GP_{1/2}$.[34] More importantly, with the loading of the third-layer of rGO, the length of the line tail further extends to a higher position as shown in Fig. S6(c) (ESI†), implying the enhancement of conductive loss. It is consistent with the increasing tendency of electrical conductivity for the hierarchical composite foams as depicted in Fig. S6(d) (ESI†). The conductive loss plays a crucial role in microwave dissipation as time-dependent electromagnetic field-induced currents occur in the conductive network.[12] Additionally, similar phenomena can be observed for the other $PI–GP_x–rGO$ with different second layers (rGO/PI_x, Fig. S6(e) and (f) (ESI†)). Therefore, the aforementioned results reveal that two main facts, including the interfacial polarization relaxation of multi-hierarchical structures and the conductive loss of the rGO network, synergistically endow the $PI–GP_x–rGO$ composite foam with excellent dielectric loss.

Microwave absorption properties of composite foams

To investigate the microwave absorption performance of the foams, the reflection loss (RL) of the incident electromagnetic wave was calculated according to eqn (1) and (2):

$$\text{RL (dB)} = 20 \log \left| \frac{Z_{in} - Z_0}{Z_{in} + Z_0} \right| \quad (1)$$

$$Z_{in} = Z_0 \sqrt{\frac{\mu_r}{\varepsilon_r}} \tanh \left[j \left(\frac{2\pi f d}{c} \right) \sqrt{\mu_r \varepsilon_r} \right] \quad (2)$$

where μ_r and ε_r are the relative permeability and permittivity of the composites, respectively, f is the microwave frequency, d is the thickness of the composites and c is the speed of light.[11,15,35] The values of reflection loss are displayed in Fig. 5, 7 and Fig. S7, S8 (ESI†).

As shown in Fig. 5(d), the pure rGO foam has an RL_{min} value of −14 dB when the absorber thickness and frequency are 5 mm and 9.81 GHz, respectively. Its effective bandwidth (RL < −10 dB) is 3.73 GHz (8.16–11.89 GHz). However, the MA performance of PI is poor over the entire frequency range (Fig. 5(a)). After being combined with $rGO/PI_{1/2}$, the RL_{min} value of the $PI–GP_{1/2}$ foam can be effectively decreased to −20.15 dB at 8.16 GHz when the thickness is 5 mm (as displayed in Fig. 5(b) and Fig. S7, ESI†). At this time, its effective bandwidth is 3.73 GHz (6.67–10.40 GHz). As for $PI–GP_{1/2}–rGO$ (Fig. 5(c) and Fig. S7, ESI†), an RL_{min} value of −24.86 dB at 18.0 GHz with a thickness of 2 mm is obtained, while the effective bandwidth is improved to 3.97 GHz (14.03–18 GHz). In comparison with $PI–GP_{1/2}$ and pure rGO foams, the conspicuous enhancement in absorption capacity and bandwidth can be attributed to the successful construction of the three-level impedance gradient in the foam.

On one hand, the introduction of the third-layer rGO will promote the formation of conductive networks on the surface of the $PI–GP_{1/2}$ skeleton, leading to the generation of a strong random multiple reflection loss in the final composite foam. On the other hand, the effective construction of the three-level impedance gradient in $PI–GP_{1/2}–rGO$ will further improve the attenuation of electromagnetic waves entering the skeleton structure interior (through the rGO on the surface) in comparison with the monotonous rGO foam.

Based on eqn (2), the normalized characteristic impedance ($Z = |Z_{in}/Z_0|$) can be calculated to evaluate the impedance matching of the composite foams.[36] As a result, the two-dimensional (2D) impedance matching contour maps of
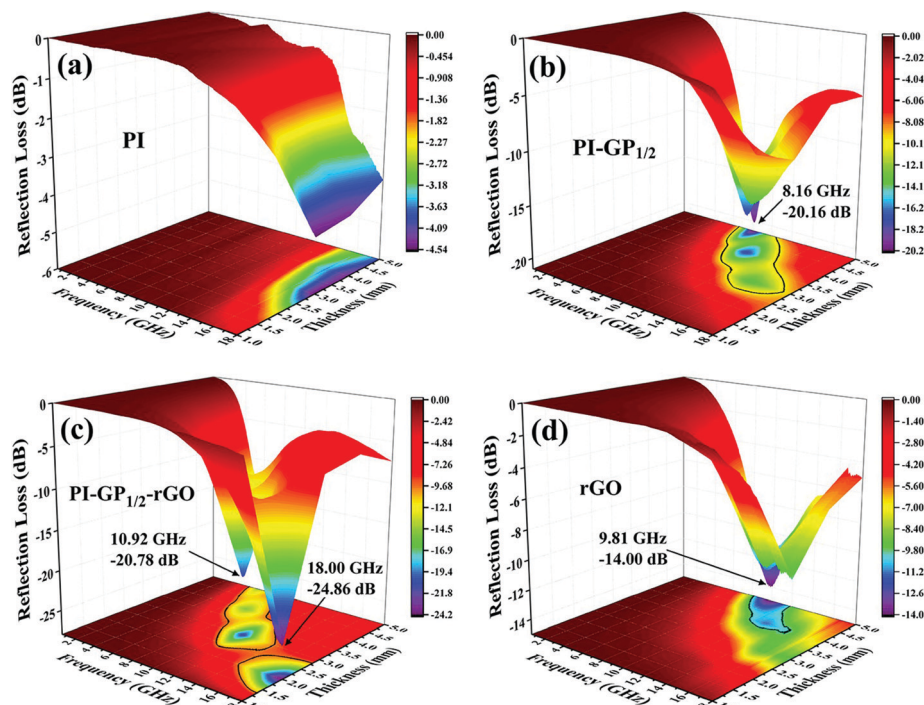
Fig. 5 3D reflection loss maps of composite foams: (a) PI, (b) PI–GP$_{1/2}$, (c) PI–GP$_{1/2}$–rGO and (d) rGO.

PI–GP$_{1/2}$–rGO and pure rGO with sample thickness and measurement frequency are exhibited in Fig. 6(a) and (b), respectively. The color of sky blue represents the area in which Z equals 1. Therefore, achieving good impedance matching requires that the value of Z is equal or close to 1. In comparison with rGO, PI–GP$_{1/2}$–rGO exhibits conspicuous optimization in impedance matching due to the introduction of the hierarchical structure (PI and GP$_{1/2}$), meaning that the more incident electromagnetic waves could
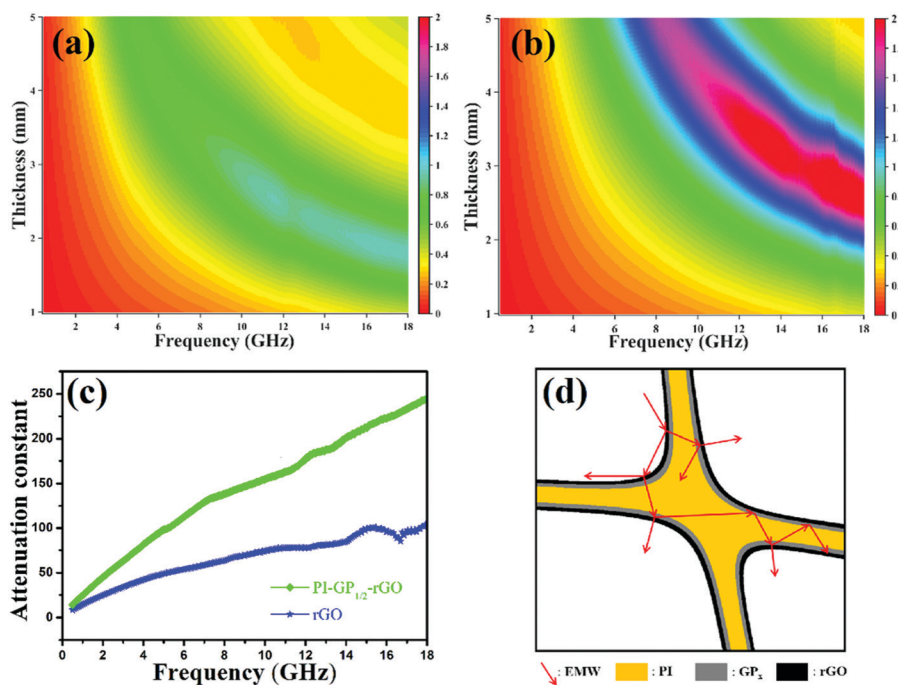

Fig. 6 2D impedance matching contour maps ($|Z_{in}/Z_0|$) of the composite foams with different thicknesses from 0.5 GHz to 18 GHz: (a) PI–GP$_{1/2}$–rGO and (b) rGO; (c) attenuation constants of the composite foams; and (d) illustration of EMW absorption mechanisms for the PI–GP$_x$–rGO composite foams.
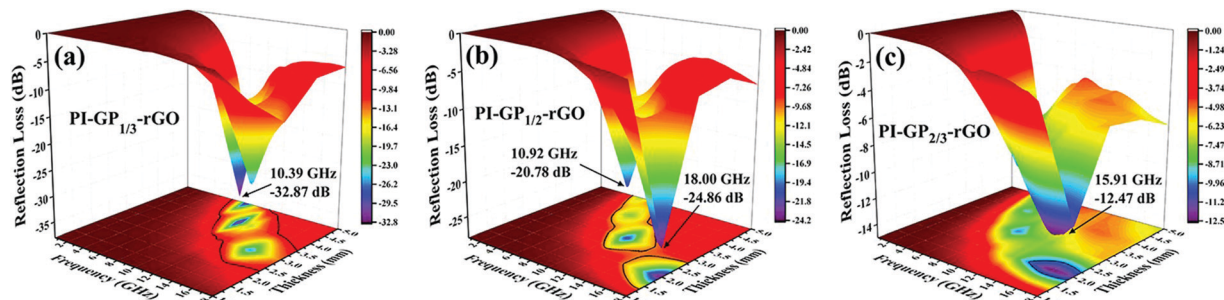
Fig. 7 3D reflection loss maps of composite foams: (a) PI–GP$_{1/3}$–rGO, (b) PI–GP$_{1/2}$–rGO and (c) PI–GP$_{2/3}$–rGO.

enter the absorber. Meanwhile, the attenuation constant is also used to qualify the electromagnetic energy attenuation ability of the absorber, which can be calculated using eqn (3):

$$\alpha = \frac{\sqrt{2}\pi f}{c}\sqrt{(\mu''\varepsilon'' - \mu'\varepsilon') + \sqrt{(\mu''\varepsilon'' - \mu'\varepsilon')^2 + (\mu''\varepsilon' + \mu'\varepsilon'')^2}} \quad (3)$$

As shown in Fig. 6(c), PI–GP$_{1/2}$–rGO exhibits a higher EMW attenuation constant than the pure rGO foam, which is beneficial to enhance the attenuation of incident EMWs as much as possible. As a consequence, the EMWs can be dissipated as intrinsic conductive/dielectric loss and multiple reflection/scattering between the internal interfaces of the composite skeleton as demonstrated in Fig. 6(d), thereby exhibiting an excellent microwave absorption performance.

Furthermore, on the basis of the same multi-hierarchical configuration, the optimization of impedance gradient for the composite foams will become an efficient means for realizing the

controllable adjustment of microwave absorption performance. As shown in Fig. 7 and Fig. S8 (ESI†), with the decrease of GO content in the second-layer GO/PAA$_x$, the RL_{min} value of PI–GP$_x$–rGO shows a tendency to decrease from −12.47 dB (PI–GP$_{2/3}$–rGO) to −24.86 dB (PI–GP$_{1/2}$–rGO), and −32.87 dB (PI–GP$_{1/3}$–rGO), whereas the corresponding effective bandwidth decreases from 4.51 GHz to 3.97 GHz, and then increases to a higher value of 6.22 GHz.

Compared with PI–GP$_{1/2}$–rGO and PI–GP$_{2/3}$–rGO, the attenuation constant of PI–GP$_{1/3}$–rGO is lower than those of PI–GP$_{1/2}$–rGO and PI–GP$_{2/3}$–rGO with the increasing GO content in the second-layer GP$_x$ (Fig. 8(d)), whereas the impedance matching for PI–GP$_{1/3}$–rGO shows a reverse improvement as displayed in Fig. 8(a)–(c). Under the synergistic effect of impedance matching and attenuation characteristics, a valley of MA performance (corresponding effective bandwidth) arises for the sample of PI-GP$_{1/2}$–rGO (3.97 GHz), which is lower than that of PI–GP$_{2/3}$–rGO (4.51 GHz) and PI–GP$_{1/3}$–rGO (6.22 GHz).
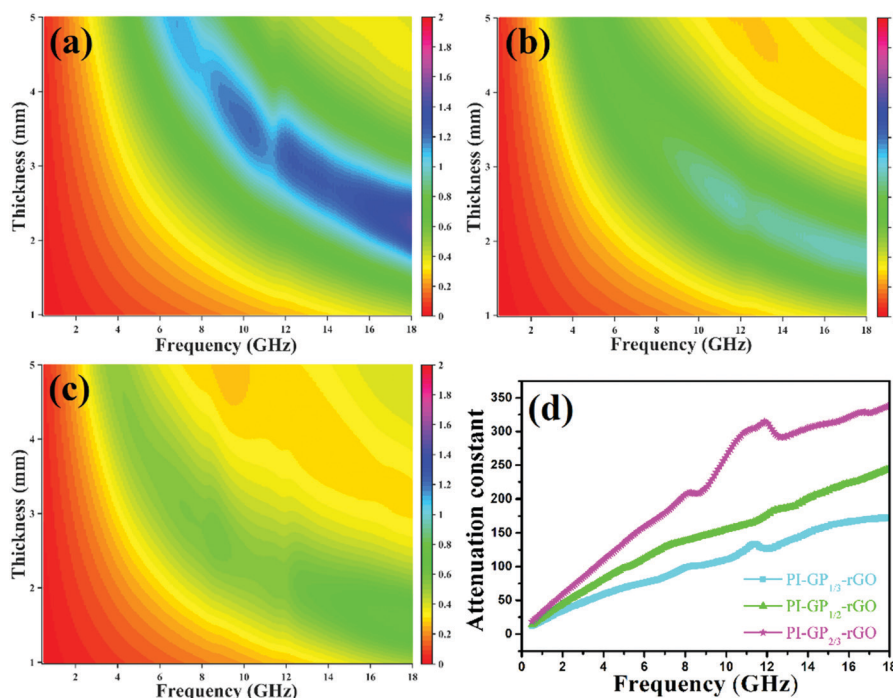

Fig. 8 2D impedance matching contour maps ($|Z_{in}/Z_0|$) of composite foams with different thicknesses from 0.5 GHz to 18 GHz: (a) PI–GP$_{1/3}$–rGO; (b) PI–GP$_{1/2}$–rGO and (c) PI–GP$_{2/3}$–rGO. (d) Attenuation constants of the composite foams.

Table 2 Microwave absorption performance of the recently reported carbon-based materials

	Density (mg cm^{-3})	Thickness (mm)	RL_{min} (dB)	Effective bandwidth (GHz)	Frequency range (GHz)	Ref.
Graphene aerogel	4.76	5.0	−14.0	3.73	8.16–11.89	12
HOPG	5 wt%	2.0	−18.0	4.5	11.7–16.2	18
Fe$_3$O$_4$/ZIF-67@WA	150	1.5	−23.4	4.5	13.5–18.0	37
Porous graphene	40–50	2.0	−27.9	5.59	12.41–18.0	38
Ni/carbon foam	100	2.0	−45.0	4.60	11.4–16.0	39
PI–GP$_{1/3}$–rGO	63.7	4.0	−32.9	6.22	8.26–14.48	This work

Therefore, it can be concluded that, under the synergistic effect of impedance matching and attenuation characteristics, good impedance matching will play a crucial role in facilitating the entry of more incident electromagnetic waves into the absorber and the dissipation of incident EMWs as much as possible.

Table 2 lists the recently reported porous carbon materials and their corresponding MA performance in the frequency range of 0.5–18 GHz.[12,18,37–39] As shown in Table 2, our PI–GP$_{1/3}$–rGO presents a distinct competitive advantage in contrast to other porous materials when the thickness is in a similar order. For example, the porous graphene with a density of 150 mg cm^{-3} exhibits an RL_{min} value of −23.4 dB and an effective bandwidth of 4.5 GHz.[37] However, the PI–GP$_{1/3}$–rGO with a lower density of 63.7 mg cm^{-3} shows a higher RL_{min} value of −32.9 dB and a broader effective bandwidth of 6.22 GHz. Moreover, similar phenomena can be observed for Ni/carbon foam and porous graphene.[38,39] As a result, the competitive superiority of PI–GP$_{1/3}$–rGO composite foam can be ascribed to the successful construction of the hierarchical impedance gradient skeleton structure, which facilitates the effective attenuation of electromagnetic waves entering the skeleton structure interior, thereby achieving the goal of broadening the bandwidth. Therefore, we can conclude that the excellent broadband microwave absorption performance combined with a low density makes it possible for PI-GP$_x$-rGO to become an efficient microwave attenuation material with great potential to be deployed in aerospace and aviation fields.

Conclusions

In summary, polyimide/graphene composite foams with a three-level impedance gradient structure have been successfully constructed by two-step vacuum impregnation. The results of SEM, TGA, and XRD confirm that the thermal treatment effectively promotes the reduction of GO sheets and the imidization of poly(amic acid) chains. The effective construction of the three-level impedance gradient further improves the attenuation of electromagnetic waves entering the skeleton structure interior. The electromagnetic waves are dissipated as intrinsic conductive/dielectric loss and internal multiple reflection/scattering between the internal interfaces of the composite skeleton, thereby endowing the composite foam with excellent broadband microwave absorption performance. Meanwhile, microwave absorption performance can be controllably adjusted by optimizing the permittivity properties of

the second-layer GO/PAA$_x$ with different GO contents. As a consequence, PI–GP$_{1/3}$–rGO exhibits an excellent RL_{min} value of −32.87 dB with a broad effective bandwidth of 6.22 GHz (8.26–14.48 GHz) at 10.39 GHz when the absorber thickness is 4.0 mm, which makes it promising to become an efficient microwave absorption material with a distinct competitive advantage.

Conflicts of interest

There are no conflicts to declare.

Note added after first publication

This article replaces the version published on 19th January 2021, in which Fig. 1 was erroneously replaced with a duplicate of Scheme 1.

Acknowledgements

References

1 D. Q. Zhang, H. B. Zhang, J. Y. Cheng, H. Raza, T. T. Liu, B. Liu, X. W. Ba, G. P. Zheng, G. H. Chen and M. S. Cao, *J. Mater. Chem. C*, 2020, **8**, 5923–5933.

2 H. G. Wang, F. B. Meng, J. Y. Li, T. Li, Z. J. Chen, H. B. Luo and Z. W. Zhou, *ACS Sustainable Chem. Eng.*, 2018, **6**, 11801–11810.

3 D. A. Gopakumar, A. R. Pai, Y. B. Pottathara, D. Pasquini, d. M. L. Carlos, M. Luke, N. Kalarikkal, Y. Grohens and S. Thomas, *ACS Appl. Mater. Interfaces*, 2018, **10**, 20032–20043.

4 T. Li, D. D. Zhi, Y. Chen, B. Li, Z. W. Zhou and F. B. Meng, *Nano Res.*, 2020, **13**, 477–484.

5 Q. Hu, Y. Fang, J. J. Wang, Z. Du, Q. Q. Song, Z. L. Guo, Y. Huang, J. Lin and C. C. Tang, *J. Mater. Chem. C*, 2019, 7, 13878–13886.

6 W. C. Li, L. Y. Xu, X. Zhang, Y. Gong, Y. Ying, J. Yu, J. W. Zheng, L. Qiao and S. L. Che, *Compos. Commun.*, 2020, **19**, 182–188.

7 Z. Xiang, J. Xiong, B. W. Deng, E. B. Cui, L. Z. Yu, Q. W. Zeng, K. Pei, R. C. Che and W. Lu, *J. Mater. Chem. C*, 2020, **8**, 2123–2134.

8 L. Y. Liang, R. S. Yang, G. J. Han, Y. Z. Feng, B. Zhao, R. Zhang, Y. M. Wang and C. T. Liu, *ACS Appl. Mater. Interfaces*, 2020, **12**, 2644–2654.

9 Y. Y. Wang, Z. H. Zhou, C. G. Zhou, W. J. Sun, J. F. Gao, K. Dai, D. X. Yan and Z. M. Li, *ACS Appl. Mater. Interfaces*, 2020, **12**, 8704–8712.

10 M. Hamidinejad, B. Zhao, A. Zandieh, N. Moghimian, T. Filleter and C. B. Park, *ACS Appl. Mater. Interfaces*, 2018, **10**, 30752–30761.

11 X. L. Li, X. W. Yin, H. L. Xu, M. K. Han, M. H. Li, S. Liang, L. F. Cheng and L. T. Zhang, *ACS Appl. Mater. Interfaces*, 2018, **10**, 34524–34533.

12 Z. C. Wang, R. B. Wei, J. W. Gu, H. Liu, C. T. Liu, C. J. Luo, J. Kong, Q. Shao, N. Wang, Z. H. Guo and X. B. Liu, *Carbon*, 2018, **139**, 1126–1135.

13 F. B. Meng, H. G. Wang, W. Wei, Z. J. Chen, T. Li, C. Y. Li, Y. Xuan and Z. W. Zhou, *Nano Res.*, 2018, **11**, 2847–2861.

14 M. Antunes and J. I. Velasco, *Prog. Polym. Sci.*, 2014, **39**, 486–509.

15 B. Zhao, J. S. Deng, C. X. Zhao, C. D. Wang, Y. G. Chen, M. Hamidinejad, R. S. Li and C. B. Park, *J. Mater. Chem. C*, 2020, **8**, 58–70.

16 B. Zhao, R. M. Wang, Y. Li, Y. M. Ren, X. Li, X. Q. Guo, R. Zhang and C. B. Park, *J. Mater. Chem. C*, 2020, **8**, 7401–7410.

17 Y. Zhang, Y. Huang, H. H. Chen, Z. Y. Huang, Y. Yang, P. S. Xiao, Y. Zhou and Y. S. Chen, *Carbon*, 2016, **105**, 438–447.

18 W. L. Song, M. S. Cao, L. Z. Fan, M. M. Lu, Y. Li, C. Y. Wang and H. F. Ju, *Carbon*, 2014, **77**, 130–142.

19 S. Wang, N. Xiao, Y. Zhou, Z. Ling, M. Li and J. Qiu, *Carbon*, 2016, **105**, 224–226.

20 A. Sheng, W. Ren, Y. Q. Yang, D. X. Yan, H. J. Duan, G. Z. Zhao, Y. Q. Liu and Z. M. Li, *Composites, Part A*, 2020, **129**, 105692.

21 W. L. Song, C. C. Gong, H. M. Li, X. D. Cheng, M. J. Chen, X. J. Yuan, H. S. Chen, Y. Z. Yang and D. N. Fang, *ACS Appl. Mater. Interfaces*, 2017, **9**, 36119–36129.

22 Y. D. Xu, Y. Q. Yang, D. X. Yan, H. J. Duan, G. Z. Zhao and Y. Q. Liu, *ACS Appl. Mater. Interfaces*, 2018, **10**, 19143.

23 X. L. Li, X. W. Yin, C. Q. Song, M. K. Han, H. L. Xu, W. Y. Duan, L. F. Cheng and L. T. Zhang, *Adv. Funct. Mater.*, 2018, **28**, 1803938.

24 H. J. Duan, H. X. Zhu, J. F. Gao, D. X. Yan, K. Dai, Y. Q. Yang, G. Z. Zhao, Y. Q. Liu and Z. M. Li, *J. Mater. Chem. A*, 2020, **8**, 9146–9159.

25 H. N. Li, L. Xu, S. Hansinee, W. Kimal and Y. Cheng, *Compos. Commun.*, 2016, **1**, 48–53.

26 C. Daniela, D. V. K. Marcano, J. M. Berlin, A. Sinitskii, Z. Z. Sun, A. Slesarev, L. B. Alemany, W. Lu and J. M. Tour, *ACS Nano*, 2010, **4**, 4806–4814.

27 L. Li, Y. Zhang, H. Y. Lu, Y. F. Wang, J. S. Xu, J. X. Zhu, C. Zhang and T. X. Liu, *Nat. Commun.*, 2020, **11**, 62.

28 K. P. Ruan, Y. Q. Guo, Y. S. Tang, Y. L. Zhang, J. N. Zhang, M. K. He, J. Kong and J. W. Gu, *Compos. Commun.*, 2018, **10**, 68–72.

29 Y. Y. Wang, Z. H. Zhou, C. G. Zhou, W. J. Sun, J. F. Gao, K. Dai, D. X. Yan and Z. M. Li, *ACS Appl. Mater. Interfaces*, 2020, **12**, 8704–8712.

30 Y. C. Qing, Q. L. Wen, F. Luo and W. C. Zhou, *J. Mater. Chem. C*, 2016, **4**, 4853–4862.

31 H. D. Huang, C. Y. Liu, D. Zhou, X. Jiang, G. J. Zhong, D. X. Yan and Z. M. Li, *J. Mater. Chem. A*, 2015, **3**, 4983–4991.

32 J. W. Li, Y. Q. Ding, N. Yu, Q. Gao, X. Fan, X. Wei, G. C. Zhang, Z. L. Ma and X. H. He, *Carbon*, 2020, **158**, 45–54.

33 H. Kim, Y. Miura and C. W. Macosko, *Chem. Mater.*, 2010, **22**, 3441–3450.

34 X. N. Chen, Y. Zhang, L. Tao, Q. Q. Nie, F. C. Meng, S. B. Zhu, L. Y. Cui and R. X. Huang, *Carbon*, 2020, **164**, 224–234.

35 P. A. Miles, W. B. Westphal and A. Von Hippel, *Rev. Mod. Phys.*, 1957, **29**, 279.

36 B. W. Deng, Z. Xiang, J. Xiong, Z. C. Liu, L. Z. Yu and W. Lu, *Nano-Micro Lett.*, 2020, **12**, 55.

37 L. L. Xu, Y. Xiong, B. K. Dang, Z. N. Ye, C. D. Jin, Q. F. Sun and X. H. Yu, *Mater. Des.*, 2019, **182**, 108006.

38 C. Chen, J. B. Xi, E. Z. Zhou, L. Peng, Z. C. Chen and C. Gao, *Nano-Micro Lett.*, 2018, **10**, 26.

39 H. B. Zhao, Z. B. Fu, H. B. Chen, M. L. Zhong and C. Y. Wang, *ACS Appl. Mater. Interfaces*, 2016, **8**, 1468–1477.

2094 | *J. Mater. Chem. C*, 2021, **9**, 2086–2094

This journal is © The Royal Society of Chemistry 2021